

Bottom-up and top-down reasoning with convolutional latent-variable models

Peiyun Hu
UC Irvine

peiyunh@ics.uci.edu

Deva Ramanan
UC Irvine

dramanan@ics.uci.edu

Abstract

Convolutional neural nets (CNNs) have demonstrated remarkable performance in recent history. Such approaches tend to work in a “unidirectional” bottom-up feed-forward fashion. However, biological evidence suggests that feedback plays a crucial role, particularly for detailed spatial understanding tasks. This work introduces “bidirectional” architectures that also reason with top-down feedback: neural units are influenced by both lower and higher-level units. We do so by treating units as latent variables in a global energy function. We call our models convolutional latent-variable models (CLVMs). From a theoretical perspective, CLVMs unify several approaches for recognition, including CNNs, generative deep models (e.g., Boltzmann machines), and discriminative latent-variable models (e.g., DPMs).

From a practical perspective, CLVMs are particularly well-suited for multi-task learning. We describe a single architecture that simultaneously achieves state-of-the-art accuracy for tasks spanning both high-level recognition (part detection/localization) and low-level grouping (pixel segmentation). Bidirectional reasoning is particularly helpful for detailed low-level tasks, since they can take advantage of top-down feedback. Our architectures are quite efficient, capable of processing an image in milliseconds. We present results on benchmark datasets with both part/keypoint labels and segmentation masks (such as PASCAL and LFW) that demonstrate a significant improvement over prior art, in both speed and accuracy.

1. Introduction

Convolutional neural nets (CNN’s), pioneered by Le-Cun *et al.* [34], have demonstrated remarkable performance in recent history [30, 43, 47]. One attractive property is their ability to transfer knowledge across tasks: CNN’s trained for image classification perform well for object detection [8], image captioning [27], and pose estimation [4], among other tasks [40]. Often, this requires a small amount of “fine-tuning”. A tantalizing question is whether a *universal “off-the-shelf” feature extractor* could support a wide

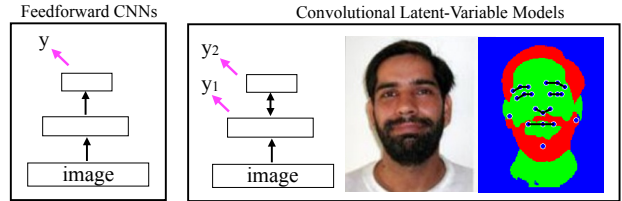


Figure 1: Traditional feed-forward neural architectures produce a target prediction for a high-level task (such as image classification) using features extracted from a high neural layer (**left**). We introduce latent variable models that incorporate top-down feedback, where lower variable activations are influenced by higher variables. Such architectures can produce state-of-the-art features for high-level tasks (like keypoint detection/localization) and low-level tasks (like pixel segmentation). We show an example of predictions for both facial keypoint localization and pixel-segmentation on the **right** image.

range of tasks from high-level recognition to low-level pixel grouping.

Feedback: Human physiology strongly suggests the existence of such a universal feature hierarchy [31]. Hochstein and Ahissar [19] present evidence that *vision at a glance* tasks, such as rapid scene categorization [49], can be computed with feedforward hierarchical processing. However, *vision with scrutiny* tasks, such as fine-grained categorization [28] or detailed spatial manipulations [22], appear to require feedback along a “reverse hierarchy”. For example, low-level V1 neurons tuned for local features (such as oriented edges) can adapt to a global figure-ground mask after 40ms [33, 57]. Indeed, *most* neural connections in the visual cortex are believed to be feedback rather than feed-forward [5, 31]. We take away two conclusions from these observations: (1) a universal architecture capable of coarse and fine tasks will likely require feedback and (2) feedback can occur fairly rapidly (within 100ms).

Boltzmann machines: To begin our discussion, we appeal to mathematical models that *are* capable of bidirectional reasoning. One elegant approach is that of hierarchical probabilistic models [23, 35, 55]. Boltzmann ma-

chines [1] can be seen as the generative probabilistic deep “counterpart” to CNNs. Importantly, neural units in deep Boltzmann machines are influenced by those in layers below *and above* [41]. The basic mechanism for accomplishing this is a (normalized) global energy function linking all units together. Though quite attractive, such models have not enjoyed the empirical success of discriminatively-trained, feed-forward counterparts.

Part models: In principle, global energy (or scoring) functions could be trained discriminatively. This is the basis for much of structured prediction, including the widely-used deformable part model (DPM) [6]. Interestingly, feed-forward inference on DPMs can be written as a CNN [9]. But our interest in DPMs stems their ability for top-down feedback: a high-level “root” object can influence the activation of a lower-level “part”. Such models were state-of-the-art until recently, but appear to have saturated because learning deep hierarchies of parts remains challenging.

Overview: We introduce a convolutional latent variable model (CLVM) that unifies these representations. CLVMs are defined over a global scoring function (like a Boltzmann machine), but with convolutionally tied weights (like a CNN). The global scoring function is *not* probabilistically normalized, and instead is discriminatively trained with supervision (like a DPM). Crucially, CLVMs can be implemented with modifications to existing deep learning toolboxes, allowing one to make use of optimized routines for gradient-based learning. After describing our model in detail, we compare it to related work in deep learning in Sec. 2.

Related work: (joint recognition and grouping) There has been a considerable amount of work integrating high-level recognition with low-level grouping cues. One approach is top-down guided segmentation: for example, one can prime a low-level pixel segmentation engine with top-down cues from an object detector [2, 3, 32, 53]. Other approaches use bottom-up proposals to prime object detections [8, 13]. In either case, recognition and grouping steps are typically treated as separate stages in a pipeline, making it difficult to perform end-to-end multi-task training (unlike CLVMs).

2. Latent variable model

In this section, we introduce our convolutional latent-variable models (CLVMs). We begin with a high-level overview. Variables will be organized into layers, spatial locations, and channels (much like the neural activations of a CNN). CLVMs are optimized by layer-wise coordinate descent through convolution, rectification, and pooling-like operations. These operations are similar to those in contemporary CNNs, but crucially differ in that they allow for top-down feedback. We will explore the theoretical relationship between CNNs and CLVMs in detail.

To begin our discussion, let us recall the central *neurody-*

namic equation governing the activation of a single “neural unit” z_i [15]:

$$z_i = \phi(b_i + \sum_{j \neq i} w_{ij} z_j) \quad (1)$$

where b_i is a bias, w_{ij} are weights between units i and j that define excitatory or inhibitory interactions depending on their sign and magnitude. Importantly, ϕ is a non-linear activation function. Ackley *et al.* [1] point out that when the activation is a sigmoid function, (1) can be seen as stochastic updates for a global probabilistic model known as a Boltzmann machine:¹

$$\begin{aligned} \phi_{\text{sig}}(x) &= \frac{1}{1 + e^{-x}} \Rightarrow P(z) \propto e^{S_{\text{Boltz}}(z)} \quad \text{where} \\ S_{\text{Boltz}}(z) &= \frac{1}{2} z^T W z + b^T z, \quad z_i \in \{0, 1\}, w_{ii} = 0 \end{aligned} \quad (2)$$

where $W = [w_{ij}]$, $z = [z_i]$, and $b = [b_i]$. Here, units z are treated as binary latent variables that capture the absence or presence of various features. Importantly, these variables are linked in a globally consistent scoring function that captures bidirectional interactions between variables encoded in the symmetric matrix W . This coupling allows low-level features (e.g., edges) to effect high-level features (e.g., objects) and vice-versa. While conceptually attractive, such models are difficult to train in practice, typically requiring sampling approximations such as contrastive divergence [16].

Let us replace the sigmoid with a simple rectified linear (ReLU) activation, common in contemporary deep networks [10, 38]. We will show that associated neural updates correspond to coordinate descent optimization of a global scoring function that is similar to $S_{\text{Boltz}}(z)$:

$$\begin{aligned} z_i &= \max(0, b_i + \sum_{j \neq i} w_{ij} z_j) \Rightarrow \max_{z \geq 0} S(z) \quad \text{where} \\ S(z) &= \frac{1}{2} z^T W z + b^T z, \quad z_i \in R^+, w_{ii} = -1 \end{aligned} \quad (3)$$

There are two important differences between $S(z)$ and $S_{\text{Boltz}}(z)$. First, latent variables z are no longer binary, but non-negative real numbers. Intuitively, they can be interpreted as capturing the absence or presence of a feature, and if present, the strength of its activation (possibly emulating the firing rate of a neuron [26]). Second, a quadratic term is added to the diagonal of W that acts as a regularizer, penalizing large activations of z . (3) is a quadratic function subject to non-negativity constraints, which is readily recognized as a quadratic program (QP).

Inference: Let us optimize (3) with coordinate ascent, solving for a single z_i holding all others fixed. Maximizing

¹One can also derive deterministic Boltzmann machine updates of the form from (1) using mean-field variational inference algorithms [24, 39].

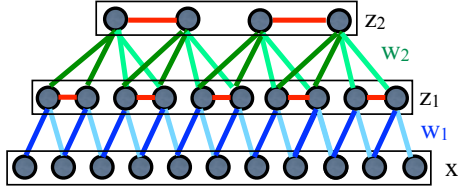


Figure 2: A convolutional latent-variable model (CLVM). Latent variables z_i are denoted by circles, arranged into layers and spatial locations. We write x for the input image and w_i for convolutional weights connecting layer $i - 1$ to i . Lateral inhibitory connections between latent variables are drawn in red. Layer-wise coordinate updates are computed by filtering, rectification, and non-maximal suppression.

a 1-d quadratic function subject to non-negative constraints is easily done by solving for the optimum and clipping:

$$\begin{aligned} \max_{z_i > 0} f(z_i) \quad \text{where} \quad f(z_i) &= -\frac{1}{2}z_i^2 + (b_i + \sum_{j \neq i} w_{ij}z_j)z_i \\ \frac{\partial f}{\partial z_i} &= -z_i + b_i + \sum_{j \neq i} w_{ij}z_j = 0 \\ z_i &= \max(0, b_i + \sum_{j \neq i} w_{ij}z_j) \end{aligned} \quad (4)$$

where (4) is exactly equivalent to (1) for a ReLU activation.

Convergence: There exist three possibilities when applying coordinate ascent; variables grow without bound, converge to a local maximum, or converge to a global maximum. Convergence is guaranteed when $(-W)$ is *copositive* [44], and a global optimum is guaranteed when $(-W)$ is positive semi-definite (PSD) [7]. A matrix A is copositive when $z^T Az \geq 0$ for all $z \geq 0$ (while PSD requires this holds for all z). Copositivity allows one to probabilistically normalize (3) into a (possibly multimodal) rectified Gaussian distribution [44], while PSD-ness allows one to rewrite (3) as a non-negative least squares problem $\min_{z \geq 0} \frac{1}{2} \|Az - y\|$ where $-W = A^T A$ and $b = A^T y$.

Inference with CNNs: State-of-the-art CNN architectures [43] actually perform coordinate-wise updates of the form from (4). With a slight abuse of notation, the input image is defined to be the (observed) bottom-most layer $x = z_0$, and the variable at layer i and spatial position u is written as $z_i[u]$. The weight connecting $z_{i-1}[u]$ to $z_i[v]$ is given by $w_i[\tau]$, where $\tau = u - v$ depends only on the relative offset between u and v (visualized in Fig. 2):

$$z_i[u] = \max(0, b_i + top_i[u] + bot_i[u]) \quad \text{where} \quad (5)$$

$$top_i[u] = \sum_{\tau} w_{i+1}[\tau] z_{i+1}[u - \tau]$$

$$bot_i[u] = \sum_{\tau} w_i[\tau] z_{i-1}[u + \tau]$$

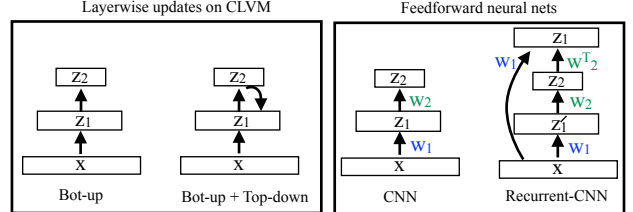


Figure 3: On the **left**, we visualize two sequences of layer-wise coordinate updates on our latent-variable model. The first is a bottom-up pass, while the second is a bottom-up + top-down pass. On the **right**, we show that bottom-up updates can be computed with a feed-forward CNN, and bottom-up-and-top-down updates can be computed with an “unrolled” CNN with additional skip connections and tied weights (which we define as a recurrent CNN). We use T to denote a 180 degree rotation of filters that maps correlation to convolution. We follow the color scheme from Fig. 2.

where we assume that layers have a single one-dimensional channel of a fixed length to simplify notation. By tying together weights such that they only depend on relative locations, bottom-up signals can be computed with cross-correlational filtering, while top-down signals can be computed with convolution. In the existing literature, these are sometimes referred to as deconvolutional and convolutional filters (related through a 180 rotation) [54]. It is natural to start coordinate updates from the bottom layer z_1 , initializing all variables to 0. During the initial bottom-up coordinate pass, top_i will always be 0. This means that the bottom-up coordinate updates can be computed with simple filtering and thresholding. *Hence a single bottom-up pass of layer-wise coordinate optimization of a CLVM can be implemented with a CNN.*

Top-down feedback: We add top-down feedback simply by applying additional coordinate updates (5) in a top-down fashion, from the top-most layer to the bottom. Fig. 3 shows that such a sequence of bottom-up and top-down updates can be “unrolled” into a feed-forward CNN with “skip” connections between layers and tied weights. One can interpret such a model as a recurrent CNN that is capable of feedback, since lower-layer variables (capturing say, edges) can now be influenced by the activations of high-layer variables (capturing say, objects). If the associated weight matrix is PSD, an infinitely-deep unrolled CNN *must* converge to a globally-optimal solution (because of the equivalence to a non-negative least squares optimization).

Non-maximal suppression (NMS): To encourage sparse activations, we add lateral inhibitory connections between groups of variables in a layer. Specifically, we write the weight connecting $z_i[u]$ and $z_i[v]$ for $(u, v) \in \text{group}$ as $w_i[u, v] = -\infty$. Such connections are shown as red edges in Fig. 2. For disjoint groups (say, non-overlapping 2x2

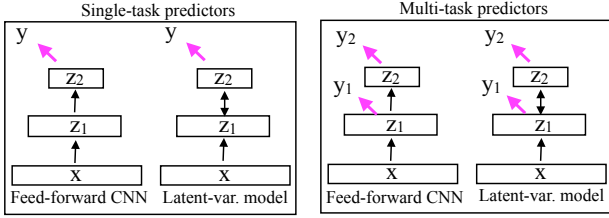


Figure 4: On the **left**, we contrast two models for single-task prediction: feed-forward CNNs versus bidirectional CLVMs (capable of top-down feedback). On the **right**, we visualize multi-task predictive models, tuned for both high-level tasks (such as part detection) and low-level tasks (such as pixel segmentation). We show that bidirectional models excel at multi-task prediction because lower-layer features become more accurate with feedback.

windows), *layer-wise updates correspond to filtering, rectification (5), and non-maximal suppression (NMS) within each group*. Unlike max-pooling, NMS encodes the spatial location of the max by returning 0 values for non-maximal locations. Standard max-pooling can be obtained as a special case by replicating filter weights w_{i+1} across variables z_i in the same pooling window (as shown in Fig. 2). This makes NMS independent of the top-down signal top_i . However, our model is more general in that NMS can be guided by top-down feedback: high-level variables (capturing objects) influence both the activation and spatial location of low-level variables (capturing edges). Interestingly, our approach seems to encode spatial information without requiring additional ‘capsule’ variables [17].

Approximate inference: Given the above global scoring function and an image x , inference corresponds to $\text{argmax}_z S(x, z)$. As argued above, this can be implemented with an infinitely-deep unrolled recurrent CNN. However, rather than optimizing the latent variables to completion, we perform a fixed number (k) of layer-wise coordinate descent updates. This is guaranteed to report back finite variables z^* for any weight matrix W (even if not copositive or PSD):

$$z^* = \mathbf{CLVM}_k(x, W, b), \quad z^* \in R^N \quad (6)$$

We write \mathbf{CLVM}_k in bold to emphasize that it is a *vector-valued function* implementing k passes of layer-wise coordinate descent, returning a vector of all N latent variables. We set $k = 1$ for a single bottom-up pass (corresponding to a standard feed-forward CNN) and $k = 2$ for an additional top-down pass.

Output prediction: We will use these N variables as features for M different tasks that span both low-level (such as pixels segmentation) and high-level tasks (such as part localization) - see Fig. 4. Because our latent variables serve as rich, multiscale description of image features, we assume

that simple linear predictors built on them will suffice:

$$y = Vz^*, \quad y \in R^M, V \in R^{M \times N} \quad (7)$$

Training: Our overall model is parameterized by (W, V, b) . Assume we are given training data pairs of images and output label vectors $\{x_i, y_i\}$. We define a training objective as follows

$$\min_{W, V, b} R(W) + R(V) + \sum_i \text{loss}(y_i, V \mathbf{CLVM}_k(x_i, W, b)) \quad (8)$$

where R are regularizer functions (we use the Frobenius matrix norm) and ‘loss’ sums the loss of our M prediction tasks (where each is scored with log or softmax loss). We optimize the above by stochastic gradient descent. Because \mathbf{CLVM}_k is a deterministic function, its gradient with respect to (W, b) can be computed by backprop on the k -times unrolled recurrent CNN (Fig. 3). We separate V from W to ensure that feature extraction does not scale with the number of output tasks (\mathbf{CLVM}_k is independent of M). During learning, we fix diagonal weights ($w_i[u, u] = -1$) and lateral inhibition weights ($w_i[u, v] = -\infty$ for $(u, v) \in \text{group}$).

Related work (learning): The use of gradient-based backpropagation to learn an unrolled model dates back to ‘backprop-through-structure’ algorithms [11, 45] and graph transducer networks [34]. More recently, such approaches were explored general graphical models [46] and Boltzmann machines [12]. Our work uses such ideas to learn CNNs with top-down feedback using an unrolled latent-variable model. Unlike past work, our latent-variable model (3) captures ReLU activations (crucial for high-performance [30]) and provides formal guarantees of optimality (for a PSD weight matrix).

Related work (top-down): Prior work has explored networks that reconstruct images given top-down cues. This is often cast as unsupervised learning with autoencoders [18, 37, 51] or deconvolutional networks [54], though supervised variants also exist [36]. Our network differs in that all nonlinear operations (rectification and max-pooling) are influenced by both bottom-up and top-down knowledge (5), which is justified from a latent-variable perspective.

3. Implementation

In this section, we provide details for implementing \mathbf{CLVM}_1 and \mathbf{CLVM}_2 with existing CNN toolboxes. We visualize our specific architecture in Fig. 5, which closely follows the bottom 8 layers of the state-of-the-art Deep19 CNN [43]: we use 3X3 filters and 2X2 non-overlapping pooling windows (for NMS). When processing NMS-layers, our model uses 6X6 replicated filters, which can be implemented with standard max-pooling and 3x3 filters (as

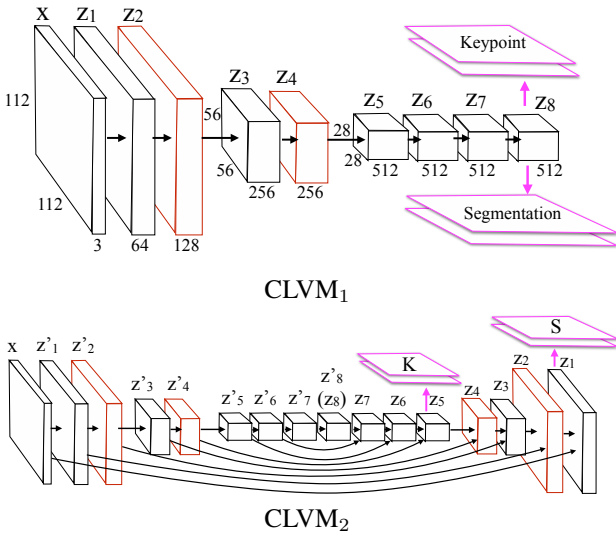


Figure 5: We show the specific CLVM networks implemented in our experiments. CLVM₁ corresponds to a standard CNN: we use the bottom 8 layers of the state-of-the-art Deep19 CNN [43]. CLVM₂ is implemented with an 2X “unrolled” recurrent CNN with transposed weights, skip connections, and zero-interlaced upsampling (as shown in Fig. 6). Red layers include lateral inhibitory connections enforced with NMS. We also visualize multi-task predictors for keypoints heatmaps and pixel segmentation labels, defined on layers selected through cross-validation. Our unrolled layers bear some resemblance to neurological “reverse hierarchical” models posited for capturing feedback [19].

argued in the previous section). Hence CLVM₁ is essentially a re-implementation of Deep19, tuned for an input image of size 112X112.

CLVM₂: Fig. 6 illustrates top-down coordinate updates, which require additional feedforward layers, skip connections, and tied weights. There is a small notational inconvenience at layers that decrease in size (z_3 and z_5). In Deep19 [43], this decrease arises from a previous max-pooling operation. Our model requires an explicit 2 \times subsampling step because it employs NMS instead of max-pooling. When this subsampled layer is later used to produce a top-down signal for a future coordinate update, variables must be zero-interlaced before applying the 180-degree rotated convolutional filters. Note that is not an approximation, but the mathematically-correct application of coordinate descent for subsampled weight connections.

Training: We learn models without pre-training, initializing all weights and biases to zero-mean Gaussians with standard deviations of .01 and .1, respectively. We use batch-normalized stochastic gradient descent [21], with

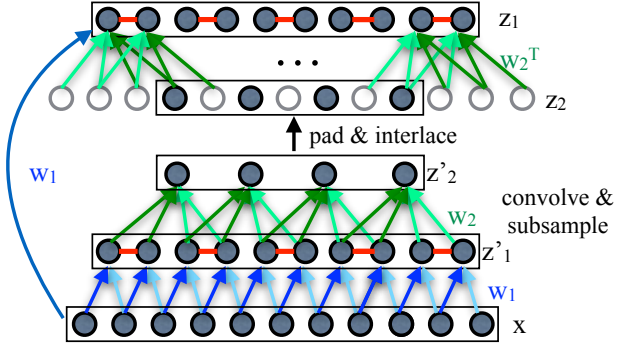
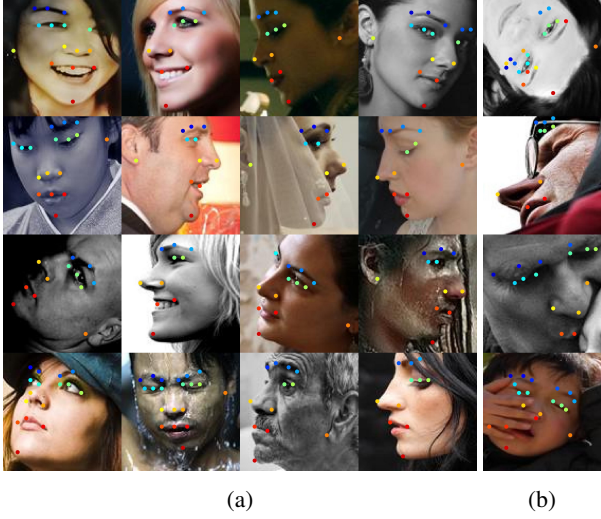


Figure 6: Two-pass layer-wise coordinate descent for a two-layer CLVM model can be implemented with modified CNN operations. White circles denote 0’s used for interlacing and border padding. We omit rectification operations to reduce clutter. We follow the color scheme from Fig. 2.

batches of size 32 and a fixed learning rate of 0.01, momentum of 0.9, and weight decay of 0.0005. All experiments are done on a single NVIDIA Tesla K40c. Our codebase is developed on top of MatConvNet [50] and will be publicly released. We implemented a custom DAG data-structure, and enforced tied weights during gradient descent by adding together gradients computed from the equivalent untied model (mathematically correct while straightforward to implement).

Supervision y_i : We experiment with single and multi-task supervision for both CLVM₁ and CLVM₂, referring to multitask variants as M-CLVM₁ and M-CLVM₂. The target label for the segmentation task is a 2D label mask that is scored with a per-pixel softmax loss (since pixels can only belong to a single class label). The target label for a single keypoint is a sparse 2D heat map with a ‘1’ at the keypoint location (or all ‘0’s if that keypoint is not visible). In practice, we dilate each keypoint map with a 3×3 mask to add jittered locations to the set of positive examples. Keypoint target maps are scored with a per-pixel log-loss (since multiple keypoints can lie at the same location).

Output classifier V : To define the output classifiers V (8), we experimented with different-size convolutional filters extracted from different layers of our model. Ideally, one could define large linear multiscale filters (that span multiple layers) and perform feature selection through learning. In practice, we do this manually by searching over single-layer filters of various sizes and layers. We optimize the layer and filter size for all models separately. We find that 5×5 filters work consistently well. For CLVM₁ and M-CLVM₁, both the segmentation and keypoint classifiers are defined on z_8 . For CLVM₂ and M-CLVM₂, z_1 is used for segmentation and z_5 for keypoints. To produce a segmentation, we take a max across all class predictions at each location. To produce keypoints, we take a max across all



(a)

(b)

Figure 7: Facial landmark localization results of CLVM₂ on AFLW, where landmark ids are denoted by color. Our bidirectional model is able to deal with large variations in appearance, pose and illumination **(a)**. We show images with extreme occlusions and pose variation in **(b)**.

locations for each predicted heatmap. By thresholding the heatmap, our system can also detect keypoints.

4. Experiment Results

To evaluate our model, we ideally need benchmark datasets with both keypoint and pixel-level annotations, which are somewhat rare. We experiment with a single-task facial keypoint dataset (AFLW), a multi-task facial keypoint+pixel dataset (LFW-Part Labels) and a multi-task human-body keypoint+pixel dataset (Pascal Person). In all cases, we assume that detections are given, either making use of ground-truth bounding boxes or off-the-shelf detectors. We resize detection windows to 112×112 (padded to 180×180 for LFW-Parts to include the background) pixels before feeding into our models. We report an oracle upper bound computed from the ideal heat map, revealing the loss in accuracy due to spatial quantization. Recall that CLVM₁ is essentially a re-implementation of the bottom 8 layers of the state-of-the-art Deep19 CNN [43], and so represents quite a strong baseline. In all cases, we outperform both our baselines and prior art, sometimes approaching the oracle performance.

AFLW: The AFLW dataset [29] is a large-scale real-world collection of 25,993 faces in 21,997 real-world images, annotated with facial keypoints. We randomly select 1000 faces for validation, 1000 for testing, and the rest for training. Notably, these faces are not limited to be responses of an existing face detector, and so this dataset contains more pose variation than other landmark datasets. We hypothesized that such pose variation might still illustrate the

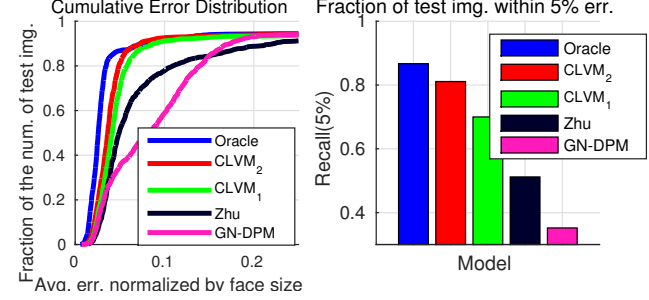


Figure 8: We plot average pixel localization error in AFLW, normalized by face size [56]. Because there are no segmentation labels, we compare only our single-task models CLVM₁ with CLVM₂ to recent state-of-the-art landmark localization systems (Zhu [56] and GN-DPM [48]). We learn a linear regressor to map the output of each method to a common subset of facial keypoints. The oracle upper-bound selects the minimum error location in the predicted heat map. We find that top-down feedback (CLVM₂) helps for even single-task prediction, producing a noticeable improvement that approaches the upper-bound.

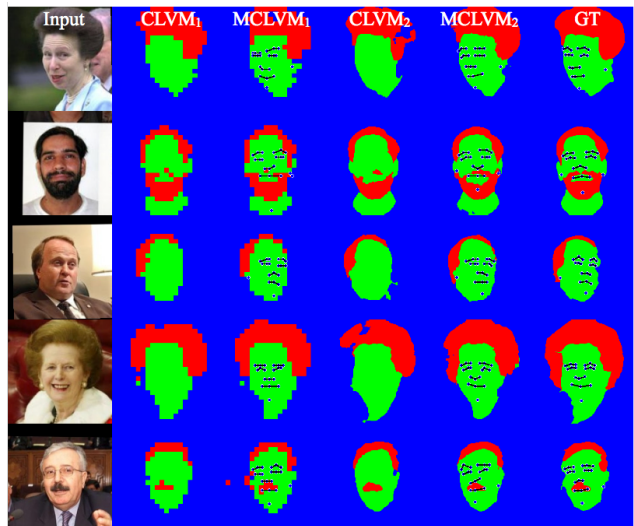


Figure 9: Segmentation and keypoint results on LFW-Parts. We use colors to denote hair (red), skin (green) and background (blue), and denote predicted keypoints with black dots. In general, bottom-up models CLVM₁ and M-CLVM₁ tend to predict pixelated segments because they use features from higher layers (that are highly nonlinear but spatially quantized). Adding top-down feedback (CLVM₂) tends to produce smoother segmentations, while multi-task training (M-CLVM₂) also removes spurious pixels.

benefit of bidirectional reasoning. We use the face detector of [56] to generate a rough bounding box labeling of each face. We visualize qualitative results in Fig. 7 and quantitative results in Fig. 8. Our CLVM models outperform state-of-the-art methods for facial keypoint estimation. In

Method	Accuracy (SP)	Error Reduction
CRF [25]	93.23%	0
Spatial CRF [25]	93.95%	10.64%
CRBM [25]	94.10%	12.85%
GLOC [25]	94.95%	25.41%
CLVM ₁	96.05%	41.60%
CLVM ₂	96.38%	46.60%
M-CLVM ₁	96.11%	42.59%
M-CLVM ₂	96.85%	53.48%
Oracle	99.97%	100.00%

Table 1: We plot superpixel-wise segmentation accuracy on LFW-Parts, following the protocol introduced in [25]. We show qualitative results in Fig. 9. We report both overall accuracy and error reduction with respect to a CRF baseline (as recommended by [25]). Our bottom-up baseline (CLVM₁) outperforms all published work. Adding top-down feedback (CLVM₂) improves results, while adding multi-task keypoint targets during learning (M-CLVM₂) produces the best overall performance. We further examine the latter model in Fig. 11 and Fig. 12.

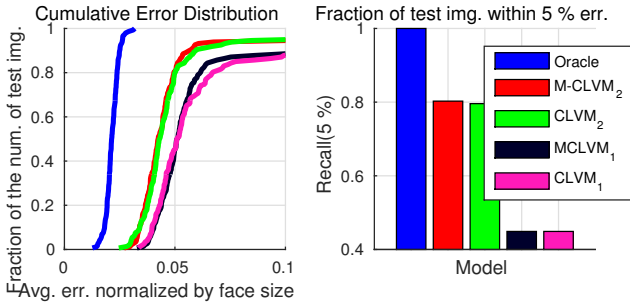


Figure 10: The **left** plots the cumulative error distribution for keypoint localization on LFW-Parts. The **right** plots the percentage of test images with an average localization error below 5%. Our two-pass models with feedback significantly outperform one-pass bottom-up variants. Multi-mask learning does not improve accuracy, but does improves speed (as we later show) because a single model can be used for diverse tasks.

fact, even the bottom-up CLVM₁ outperforms the state-of-the-art, indicating the strength of the baseline. Our two-pass CLVM₂ reduces error by another factor of 2 with respect to the upper bound. These results reveal the potential benefit of bidirectional reasoning even for a single prediction task.

LFW-Parts: LFW Parts [25] contains 2,927 face images from widely-used the LFW face dataset [20] annotated with semantic pixel labels for Hair/Skin/Background (with standard train/val/test splits). We manually annotate keypoint locations by interactively applying and correcting the land-



Figure 11: Inspired by neurological experiments [33], we show low-level activations (2 out of 64 channels from Layer 1) at two different “times”. Columns correspond to activations on different images. The **top** row of each pair visualizes z'_1 (computed at 0.5ms, during bottom-up processing), while the **bottom** visualizes z_1 (computed at 30ms, after top-down feedback). The last column shows the average channel activation of both z'_1 and z_1 . Feedback captures figure-ground information corresponding to hair (Channel 7) and skin (Channel 61). Classifiers defined on such features produce better segmentations (Fig. 12).

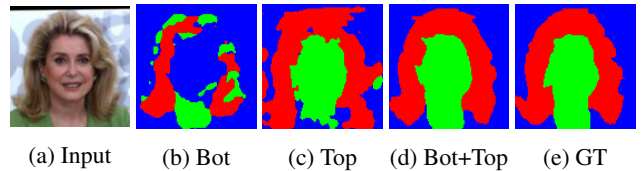
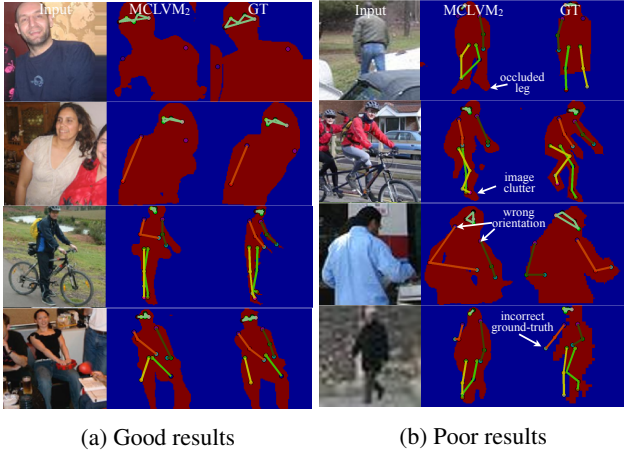


Figure 12: Given an image **(a)**, we show pixel predictions obtained with the same classifier applied to modified features $z_1 = \max(0, top_1 + bot_1)$ where the top-down and bottom-up components are artificially zero-ed out. The bottom-up-only feature **(b)** makes gross errors, missing the entire face. The top-down feature **(c)** correctly estimates coarse spatial labels but does not respect image boundaries. The final predictions **(d)** obtained by integrating both signals is closest to the ground-truth **(e)**.

mark detector trained from AFLW. Fig. 9 visualizes qualitative results, while qualitative analysis for pixel segmentation and keypoint localization are provided in Table 1 and Fig. 10. We refer the reader to the captions for a detailed analysis, but overall, we find that bidirectional top-down feedback is crucial for multi-task prediction, and that a single multi-task architecture performs as well (or even better than) multiple single-task architectures. In terms of segmentation, we reduce the best reported error [25] by a factor of 2. Fig. 11 and Fig. 12 examine our best-performing model (M-CLVM₂) in detail.



(a) Good results

(b) Poor results

Figure 13: Sample segmentation and keypoint localization results on Pascal Person. Compared to existing human pose datasets, occlusion is a significant challenge. We draw skeletons only on visible keypoints. Our models tend to produce reasonable segmentation masks and localize visible keypoints (a). On challenging images (b) with occlusions or clutter, keypoint results suffer, through segmentation masks still look reasonable. Our model also has difficulty predicting torso orientation. Poor performance can arise from incorrect annotation of ground-truth (perhaps due to low resolution instances).

Method	Accuracy (P)
Oracle	99.53%
CLVM ₁	83.40%
CLVM ₂	86.56%
M-CLVM ₁	82.91%
M-CLVM ₂	86.57%

Table 2: Pixel-wise segmentation performance on Pascal Person. Our bidirectional models significantly outperform their bottom-up counterparts. Moreover, multi-task training slightly hurts our bottom-up model (CLVM₁ vs M-CLVM₁), but slightly helps our bidirectional model (CLVM₂ vs M-CLVM₂).

Pascal Person: The Pascal 2011 Person dataset [14] consists of 7,368 person instances, each annotated with: (1) a bounding box around the visible region; (2) up to 23 human keypoints per person; and a (3) figure/ground segmentation mask. We randomly chose 70% for training, 10% for validation and 20% for testing. We evaluate localization accuracy of only visible keypoints, normalizing pixel error by the maximum side length of the instance’s visible bounding box. We compare our model against state-of-the-art pose estimation systems [52] and [42], tuned to return their best detection given the visible bounding box. Fig. 13 visual-

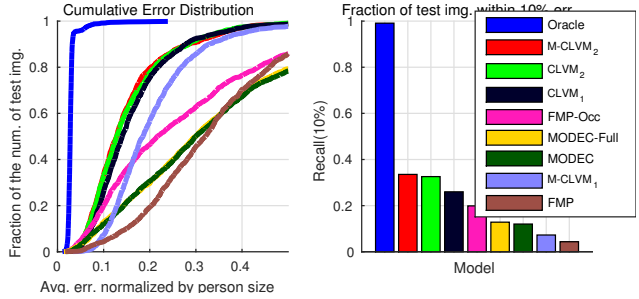


Figure 14: The **left** plot shows the cumulative error distribution for keypoints localization on Pascal Person. The **right** bar plot shows the percentage of test images that have average localization error below 10%. We evaluate localization accuracy of only visible keypoints, normalizing pixel error by the maximum side length of the instance’s visible bounding box. FMP and FMP-Occ are different versions of [52], where FPM-Occ has been re-trained on our training set. MODEC and MODEC-Full are two versions of models released by [42], where MODEC-Full is slower but better. Interestingly, multi-task learning significantly *hurts* our feed-forward models (CLVM₁ vs. M-CLVM₁), but slightly helps our bidirectional model (CLVM₂ vs. M-CLVM₂).

izes qualitative results, while quantitative analysis for pixel segmentation and keypoint localization are provided in Table 2 and Fig. 14. We refer the reader to the caption for a detailed analysis. Our CLVM models outperform prior art for keypoint localization by a large margin. Moreover, our bidirectional models strongly outperform their single-pass feedforward counterparts, particularly when evaluated on multitask prediction.

Convergence: As a diagnostic experiment, we verify that layer-wise coordinate updates do increase a global scoring function (Fig. 15). The score appears to grow unbounded, implying that the learned $(-W)$ may not be copositive. We posit that more aggressive learning may ensure convergence - e.g., directly training a network with additional unrolled layers, learning the regularization penalty (the main diagonal of W), or adding constraints during learning that enforce copositivity or PSDness. Finally, one could also ensure convergence by adding upper-bound constraints to latent variables in our global scoring function (3), through a saturating nonlinear activation function [15].

Weight-sharing: One could relax the recurrent CNN that implements our two-pass CLVM₂ model (Fig. 3) by not tying together weights across different layers. The un-tied network is strictly more flexible and can so can represent structures beyond latent-variable models. We found such models performed nearly identically to their tied counterparts while converging faster during training. Specifically, an untied M-CLVM₂ produced a super-pixel (SP) accuracy of 96.84% on LFW-Parts, just below M-CLVM₂’s perfor-

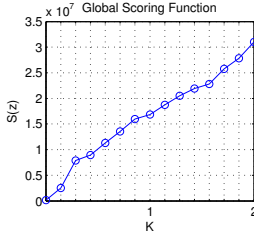


Figure 15: We plot the value of the global scoring function (3) as we perform iterations of layer-wise coordinate descent (6). Please see text for more discussion.

mance of 96.85%, both of which are noticeably better than all other variants in Table 1. Such untied networks still provide a form of feedback, and so may be interesting to examine further.

Running time: We show the running time of our models in Table 3. As expected, multi-task prediction requires essentially no additional computation over single-task prediction (which is already quite fast). Our timing results are impressive given that many of the *single-task* baselines we compare against are 100-1000 times slower.

Conclusion: We have introduced a convolutional latent-variable model (CLVM) capable of bottom-up feedforward processing and top-down feedback. CLVMs integrate several leading approaches, including CNNs, probabilistic Boltzmann machines, and discriminative latent-variable models. Both inference and learning are extremely efficient, making use of layer-wise updates that can be implemented with highly-optimized deep learning toolboxes. CLVMs produce rich multiscale features capable of supporting a diverse set of recognition tasks, including high-level keypoint localization and low-level pixel segmentation. We show that low-level *vision-with-scrutiny* tasks particularly benefit from top-down feedback. Finally, we have demonstrated impressive performance, both in terms of accuracy and speed with respect to prior art.

Acknowledgments: Funding for this research was provided by NSF Grant 0954083, ONR-MURI Grant N00014-10-1-0933, and support from Intel. This research is also supported by the Office of the Director of National Intelligence (ODNI), Intelligence Advanced Research Projects Activity (IARPA), via IARPA R & D Contract No. 2014-14071600012. The views and conclusions contained herein are those of the authors and should not be interpreted as necessarily representing the official policies or endorsements, either expressed or implied, of the ODNI, IARPA, or the U.S. Government. The U.S. Government is authorized to reproduce and distribute reprints for Governmental purposes notwithstanding any copyright annotation thereon.

References

Model	Segmentation	Keypoint
CLVM ₁	15.5 ms	13.3 ms
CLVM ₂	31.0 ms	21.5 ms
M-CLVM ₁	16.1 ms	
M-CLVM ₂	31.2 ms	

Table 3: Running times for our model on a 180×180 image. Our two-pass (feedback-aware) models are 2X slower than their feedforward counterparts. Multi-task outputs essentially come “for free”. Our multi-task models are often 100-1000 faster than many of our *single-task* baselines.

- [1] D. H. Ackley, G. E. Hinton, and T. J. Sejnowski. A learning algorithm for boltzmann machines. *Cognitive science*, 9(1):147–169, 1985.
- [2] E. Borenstein and S. Ullman. Combined top-down/bottom-up segmentation. *PAMI*, 30(12):2109–2125, 2008.
- [3] T. Brox, L. Bourdev, S. Maji, and J. Malik. Object segmentation by alignment of poselet activations to image contours. In *CVPR*, pages 2225–2232. IEEE, 2011.
- [4] X. Chen and A. L. Yuille. Articulated pose estimation by a graphical model with image dependent pairwise relations. In *NIPS*, pages 1736–1744, 2014.
- [5] R. J. Douglas, C. Koch, M. Mahowald, K. Martin, and H. H. Suarez. Recurrent excitation in neocortical circuits. *Science*, 269(5226):981–985, 1995.
- [6] P. F. Felzenszwalb, R. B. Girshick, D. McAllester, and D. Ramanan. Object detection with discriminatively trained part-based models. *PAMI*, 32(9):1627–1645, 2010.
- [7] V. Franc, V. Hlaváč, and M. Navara. Sequential coordinate-wise algorithm for the non-negative least squares problem. In *CAIP*, pages 407–414. Springer, 2005.
- [8] R. Girshick, J. Donahue, T. Darrell, and J. Malik. Rich feature hierarchies for accurate object detection and semantic segmentation. In *CVPR*, pages 580–587. IEEE, 2014.
- [9] R. Girshick, F. Iandola, T. Darrell, and J. Malik. Deformable part models are convolutional neural networks. In *CVPR*. IEEE, 2015.
- [10] X. Glorot, A. Bordes, and Y. Bengio. Deep sparse rectifier networks. In *AISTATS*, volume 15, pages 315–323, 2011.
- [11] C. Goller and A. Kuchler. Learning task-dependent distributed representations by backpropagation through structure. In *ICNN*, volume 1, pages 347–352. IEEE, 1996.
- [12] I. Goodfellow, M. Mirza, A. Courville, and Y. Bengio. Multi-prediction deep boltzmann machines. In *NIPS*, 2013.
- [13] C. Gu, J. J. Lim, P. Arbelaez, and J. Malik. Recognition using regions. In *CVPR*, pages 1030–1037. IEEE, 2009.
- [14] B. Hariharan, P. Arbelaez, L. Bourdev, S. Maji, and J. Malik. Semantic contours from inverse detectors. In *ICCV*, 2011.
- [15] S. Haykin. *Neural networks and learning machines*, volume 3. Pearson Education Upper Saddle River, 2009.
- [16] G. Hinton. Training products of experts by minimizing contrastive divergence. *Neural computation*, 14(8), 2002.
- [17] G. E. Hinton, A. Krizhevsky, and S. D. Wang. Transforming auto-encoders. In *ICANN*, pages 44–51. Springer, 2011.
- [18] G. E. Hinton and R. R. Salakhutdinov. Reducing the dimensionality of data with neural networks. *Science*, 313(5786):504–507, 2006.
- [19] S. Hochstein and M. Ahissar. View from the top: Hierarchies and reverse hierarchies in the visual system. *Neuron*, 36(5):791–804, 2002.

[20] G. B. Huang, M. Ramesh, T. Berg, and E. Learned-Miller. Labeled faces in the wild: A database for studying face recognition in unconstrained environments. Technical report, Technical Report 07-49, University of Massachusetts, Amherst, 2007.

[21] S. Ioffe and C. Szegedy. Batch normalization: Accelerating deep network training by reducing internal covariate shift. In *ICML*, 2015.

[22] M. Ito and C. D. Gilbert. Attention modulates contextual influences in the primary visual cortex of alert monkeys. *Neuron*, 22(3):593–604, 1999.

[23] Y. Jin and S. Geman. Context and hierarchy in a probabilistic image model. In *CVPR*, 2006.

[24] M. I. Jordan, Z. Ghahramani, T. S. Jaakkola, and L. K. Saul. *An introduction to variational methods for graphical models*. Springer, 1998.

[25] A. Kae, K. Sohn, H. Lee, and E. Learned-Miller. Augmenting crfs with boltzmann machine shape priors for image labeling. In *CVPR*, pages 2019–2026. IEEE, 2013.

[26] E. R. Kandel, J. H. Schwartz, T. M. Jessell, et al. *Principles of neural science*, volume 4. McGraw-Hill New York, 2000.

[27] A. Karpathy and L. Fei-Fei. Deep visual-semantic alignments for generating image descriptions. In *CVPR*, 2015.

[28] S. M. Kosslyn, W. L. Thompson, I. J. Kim, and N. M. Alpert. Topographical representations of mental images in primary visual cortex. *Nature*, 378(6556):496–498, 1995.

[29] M. Köstinger, P. Wohlhart, P. M. Roth, and H. Bischof. Annotated facial landmarks in the wild: A large-scale, real-world database for facial landmark localization. In *ICCV Workshops*, pages 2144–2151. IEEE, 2011.

[30] A. Krizhevsky, I. Sutskever, and G. E. Hinton. Imagenet classification with deep convolutional neural networks. In *NIPS*, pages 1097–1105, 2012.

[31] N. Kruger, P. Janssen, S. Kalkan, M. Lappe, A. Leonardis, J. Piater, A. J. Rodriguez-Sánchez, and L. Wiskott. Deep hierarchies in the primate visual cortex: What can we learn for computer vision? *PAMI*, 35(8):1847–1871, 2013.

[32] M. P. Kumar, P. H. Torr, and A. Zisserman. Objcut: Efficient segmentation using top-down and bottom-up cues. *PAMI*, 32(3):530–545, 2010.

[33] V. A. Lamme. The neurophysiology of figure-ground segregation in primary visual cortex. *The Journal of Neuroscience*, 15(2):1605–1615, 1995.

[34] Y. LeCun, L. Bottou, Y. Bengio, and P. Haffner. Gradient-based learning applied to document recognition. *Proceedings of the IEEE*, 86(11):2278–2324, 1998.

[35] T. S. Lee and D. Mumford. Hierarchical bayesian inference in the visual cortex. *JOSA A*, 20(7):1434–1448, 2003.

[36] J. Long, E. Shelhamer, and T. Darrell. Fully convolutional networks for semantic segmentation. In *CVPR*. IEEE, 2015.

[37] J. Masci, U. Meier, D. Cireşan, and J. Schmidhuber. Stacked convolutional auto-encoders for hierarchical feature extraction. In *ICANN*, pages 52–59. Springer, 2011.

[38] V. Nair and G. E. Hinton. Rectified linear units improve restricted boltzmann machines. In *ICML*, 2010.

[39] C. Peterson and J. Anderson. A mean field theory learning algorithm for neural networks. *Complex systems*, 1, 1987.

[40] A. S. Razavian, H. Azizpour, J. Sullivan, and S. Carlsson. Cnn features off-the-shelf: an astounding baseline for recognition. In *CVPR Workshop*, pages 512–519. IEEE, 2014.

[41] R. Salakhutdinov and G. E. Hinton. Deep boltzmann machines. In *AISTATS*, pages 448–455, 2009.

[42] B. Sapp and B. Taskar. Modec: Multimodal decomposable models for human pose estimation. In *CVPR*, 2013.

[43] K. Simonyan and A. Zisserman. Very deep convolutional networks for large-scale image recognition. In *ICLR*, 2015.

[44] N. D. Soccia, D. D. Lee, and H. Sebastian Seung. The rectified gaussian distribution. *NIPS*, pages 350–356, 1998.

[45] R. Socher, C. C. Lin, C. Manning, and A. Y. Ng. Parsing natural scenes and natural language with recursive neural networks. In *ICML*, pages 129–136, 2011.

[46] V. Stoyanov, A. Ropson, and J. Eisner. Empirical risk minimization of graphical model parameters given approximate inference, decoding, and model structure. In *AISTATS*, 2011.

[47] C. Szegedy, W. Liu, Y. Jia, P. Sermanet, S. Reed, D. Anguelov, D. Erhan, V. Vanhoucke, and A. Rabinovich. Going deeper with convolutions. In *CVPR*. IEEE, June 2015.

[48] G. Tzimiropoulos and M. Pantic. Gauss-newton deformable part models for face alignment in-the-wild. In *CVPR*, 2014.

[49] R. VanRullen and S. J. Thorpe. Is it a bird? is it a plane? ultra-rapid visual categorisation of natural and artifactual objects. *Perception-London*, 30(6):655–668, 2001.

[50] A. Vedaldi and K. Lenc. Matconvnet – convolutional neural networks for matlab. *CoRR*, abs/1412.4564, 2014.

[51] P. Vincent, H. Larochelle, I. Lajoie, Y. Bengio, and P.-A. Manzagol. Stacked denoising autoencoders: Learning useful representations in a deep network with a local denoising criterion. *JMLR*, 11:3371–3408, 2010.

[52] Y. Yang and D. Ramanan. Articulated human detection with flexible mixtures of parts. *PAMI*, 35(12):2878–2890, 2013.

[53] S. X. Yu and J. Shi. Segmentation given partial grouping constraints. *PAMI*, 26(2):173–183, 2004.

[54] M. D. Zeiler, D. Krishnan, G. W. Taylor, and R. Fergus. Deconvolutional networks. In *CVPR*, 2010.

[55] L. L. Zhu, Y. Chen, and A. Yuille. Recursive compositional models for vision: Description and review of recent work. *Journal of Mathematical Imaging and Vision*, 41(1-2):122–146, 2011.

[56] X. Zhu and D. Ramanan. Face detection, pose estimation, and landmark localization in the wild. In *CVPR*, 2012.

[57] K. Zipser, V. A. Lamme, and P. H. Schiller. Contextual modulation in primary visual cortex. *The Journal of Neuroscience*, 16(22):7376–7389, 1996.